



## Article

# The Effects of the Binder and Buffering Matrix on InSb-Based Anodes for High-Performance Rechargeable Li-Ion Batteries

Vo Pham Hoang Huy, Il Tae Kim \* and Jaehyun Hur \*

Department of Chemical and Biological Engineering, Gachon University, Seongnam 13120, Gyeonggi, Korea; vophamhoanghuy@yahoo.com.vn

\* Correspondence: itkim@gachon.ac.kr (I.T.K.); jhhur@gachon.ac.kr (J.H.);

Tel.: +82-31-750-8835 (I.T.K.); +82-31-750-5593 (J.H.)

**Abstract:** C-decorated intermetallic InSb (InSb-C) was developed as a novel high-performance anode material for lithium-ion batteries (LIBs). InSb nanoparticles synthesized via a mechanochemical reaction were characterized using X-ray diffraction (XRD), high-resolution transmission electron microscopy (HRTEM), scanning electron microscopy (SEM), X-ray photoelectron spectroscopy (XPS), and energy-dispersive X-ray spectroscopy (EDX). The effects of the binder and buffering matrix on the active InSb were investigated. Poly(acrylic acid) (PAA) was found to significantly improve the cycling stability owing to its strong hydrogen bonding. The addition of amorphous C to InSb further enhanced mechanical stability and electronic conductivity. As a result, InSb-C demonstrated good electrochemical Li-ion storage performance: a high reversible specific capacity ( $878 \text{ mAh}\cdot\text{g}^{-1}$  at  $100 \text{ mA}\cdot\text{g}^{-1}$  after 140 cycles) and good rate capability (capacity retention of 98% at  $10 \text{ A}\cdot\text{g}^{-1}$  as compared to  $0.1 \text{ A}\cdot\text{g}^{-1}$ ). The effects of PAA and C were comprehensively studied using cyclic voltammetry, differential capacity plots, ex-situ SEM, and electrochemical impedance spectroscopy (EIS). In addition, the electrochemical reaction mechanism of InSb was revealed using ex-situ XRD. InSb-C exhibited a better performance than many recently reported Sb-based electrodes; thus, it can be considered as a potential anode material in LIBs.

**Keywords:** InSb; InSb-C; PAA binder; anodes; Li-ion batteries



**Citation:** Hoang Huy, V.P.; Kim, I.T.; Hur, J. The Effects of the Binder and Buffering Matrix on InSb-Based Anodes for High-Performance Rechargeable Li-Ion Batteries. *Nanomaterials* **2021**, *11*, 3420. <https://doi.org/10.3390/nano11123420>

Academic Editor: Carlos Miguel Costa

Received: 25 November 2021

Accepted: 15 December 2021

Published: 17 December 2021

**Publisher's Note:** MDPI stays neutral with regard to jurisdictional claims in published maps and institutional affiliations.



**Copyright:** © 2021 by the authors. Licensee MDPI, Basel, Switzerland. This article is an open access article distributed under the terms and conditions of the Creative Commons Attribution (CC BY) license (<https://creativecommons.org/licenses/by/4.0/>).

## 1. Introduction

Lithium-ion batteries (LIBs) have been widely used in various portable devices and energy storage systems owing to their high energy density, high cell voltage, low self-discharge, and low memory effect [1–4]. Despite these beneficial features, current graphite anodes cannot satisfy the rapidly growing demands for their use in various applications, such as mobile devices, electrical vehicles, and large-scale grid storage systems. Therefore, the development of new anode materials with a high specific capacity, good rate capability, and long service life that can replace low theoretical capacity ( $372 \text{ mAh}\cdot\text{g}^{-1}$ ) commercial graphitic anodes is required [4–17]. Li alloys with elements, such as Si, P, Sn, and Sb, are considered to be promising anode materials because of their higher theoretical capacities (Si: 4200, P: 2595, Sn: 993, and Sb: 660  $\text{mAh}\cdot\text{g}^{-1}$ ). However, it is not straightforward to control the large volume change in these materials due to expansion/contraction during lithiation/delithiation, which leads to a deteriorated cell performance [18–23].

Recently, Sb-based materials have gained significant attention as promising anodes in LIBs owing to their low cost, high conductivity, high density, and high theoretical capacity [24–27]. Sb has higher conductivity and stability than P (the same element family) and Si (the material with the highest theoretical capacity), making it a suitable material for the development of high-performance anodes for LIBs. Because of these attractive characteristics, Sb has been intensively investigated for use in LIBs. However, satisfactory performance cannot be achieved using Sb alone because of its high-volume expansion

(135%) during the alloying reaction ( $3\text{Li}^+ + \text{Sb} \rightarrow \text{Li}_3\text{Sb}$ ) [28]. Many strategies have been proposed to resolve this problem.

The formation of a nanoscale Sb-based intermetallic alloy is an effective approach that can improve the cycling stability of Sb-based electrodes. Nanoscale active materials reduce the Li-ion diffusion pathway and alleviate the stress and strain during the electrochemical reaction. In addition, the stepwise electrochemical reaction in bimetallic Sb-based alloy nanoparticles can mitigate a large volume change relative to a pure Sb electrode. Along this line, He et al. demonstrated monodisperse colloidal SnSb nanocrystals (approximately 20 nm) with a discharge capacity of  $700 \text{ mAh}\cdot\text{g}^{-1}$  at 0.5 C after 100 cycles [29]. Yi et al. synthesized morphology-controllable Sn–Sb composites with micro- and nano-sized hollow, dendritic, or mixed-type structures; these designed composites also exhibited good cycling stability and rate performance in LIBs and sodium-ion batteries (SIBs) [29].

Another effective approach that can enhance the performance of Sb-based electrodes is to introduce various nanoscale conductive carbon materials to create nanostructured Sb/C composites (e.g., 1D carbon nanotubes, nanofibers, nanorods, 2D graphene, 3D graphite, and porous carbon) [30–33]. In this composite, carbon prevents the agglomeration of nanoparticles, increases the electrical conductivity, and reduces the volume change of the active Sb [34–36]. Therefore, the cycling stability is notably improved by adding carbon.

The binder is the crucial adhesive between the active material and conductive carbon on the current collector. The adhesion between the active component and the binder is very important during the electrochemical reaction because the stress on the active material caused by volume expansion can weaken the binding force. In a pioneering study on binder materials, Kim et al. studied the effect of a new binder material (a blend of poly(acrylic acid) (PAA) and poly(amide imide) (PAI)) on electrode adhesion and recovery characteristics. They demonstrated that the composite polymer binder exhibited superior properties compared to the individual polymers [37]. Similarly, Choi et al. developed a new polyrotaxane-based binder for active micro-silicon particle batteries in which they achieved a remarkably stable capacity of over  $3000 \text{ mAh}\cdot\text{g}^{-1}$  after 150 cycles [38]. Wu et al. have shown that conductive binders based on polyfluorene (PF) exhibit superior performance owing to their electronic conductivity and mechanical strength [39]. Among the various binders studied, PAA has shown exceptionally good performance for the Si electrode because of (i) its abundant carboxylic acid functional groups ( $-\text{COOH}$ ) that enable strong bonding to the native hydroxyl species on the Si particle surface [40,41]; (ii) good mechanical strength associated with low swelling in a liquid electrolyte [42]; and (iii) the formation of an artificial solid electrolyte interface (SEI) on the Si surface that stabilizes the electrode–electrolyte interface [43]. Accordingly, PAA is expected to be a promising binder for various anode materials with a large volume change in LIBs.

In this study, we demonstrate C-decorated InSb (InSb–C) as a novel Sb-based bimetallic high-performance anode for LIBs. InSb has been widely studied for use in transistors, magnetic sensors, and infrared photodetectors because of its semiconducting properties, which include a narrow band gap (0.17 eV), high electron mobility, and a high density of conduction states [44–46]. Although some In-based nanomaterials have been reported as good anode materials owing to the high theoretical capacity of In ( $1012 \text{ mAh}\cdot\text{g}^{-1}$ ) [27,28], intermetallic InSb has rarely been investigated as an anode material for LIBs. To achieve a high-performance InSb electrode, we investigate the effects of the binder and buffering matrix on the performance of InSb. This study demonstrates that PAA is an effective binder that impedes volume expansion and limits the structural degradation of the electrode owing to its strong hydrogen bonding with the active InSb. The addition of amorphous C reduces the stresses in InSb during lithiation/delithiation and increases the electrical conductivity. Therefore, with an appropriate binder and matrix, InSb–C exhibits high performance in terms of specific capacity, cyclic stability, and rate performance. Various characterization techniques are used to elucidate the mechanism behind the improvement, including X-ray diffraction (XRD), scanning electron microscopy (SEM), high-resolution transmission electron microscopy (HRTEM), energy-dispersive X-ray spectroscopy (EDX),

Fourier-transform infrared spectroscopy (FTIR), X-ray photoelectron spectroscopy (XPS), and electrochemical impedance spectroscopy (EIS). Furthermore, the phase transformation mechanism of InSb during lithiation/delithiation is studied using ex-situ XRD.

## 2. Experimental Section

### 2.1. Synthesis of InSb and InSb–C

InSb was synthesized using high-energy mechanical milling (HEMM). In (99.99%, Sigma-Aldrich, St. Louis, MO, USA) and Sb (99.998%, Sigma-Aldrich, St. Louis, MO, USA) powders were mixed in a 1:1 molar ratio and then placed in an 80 cm<sup>3</sup> ZrO<sub>2</sub> bowl with hardened ZrO<sub>2</sub> balls in a 20:1 ball-to-powder ratio. The mixture was milled in an Ar atmosphere for 10 h at 300 rpm. InSb–C nanocomposites were prepared using HEMM, where a mixture of as-synthesized InSb and acetylene black powder (99.9%, 100% compressed, specific surface area of 75 m<sup>2</sup>·g<sup>−1</sup>, bulk density of 170–230 g·L<sup>−1</sup>, Alfa Aesar, Catalog No. 045527, Ward Hill, MA, USA) at a mass ratio of 9:1 was milled under the same conditions as the InSb synthesis. The mechanochemical synthesis reaction for InSb–C is described as follows:



### 2.2. Material Characterization

The crystal structures of the as-prepared InSb and InSb–C were measured using powder XRD (D/MAX–2200 Rigaku, Tokyo, Japan) with Cu K $\alpha$  ( $\lambda = 1.54 \text{ \AA}$ ) radiation. The microscopic morphology of the as-synthesized powder materials was observed using HRTEM (JEOL JEM-2100F) and SEM (Hitachi S4700, Tokyo, Japan). XPS (Kratos Axis Anova, Manchester, UK) was used to evaluate the chemical states of the synthesized materials. The elemental content and distribution of the as-prepared powder and electrode after electrochemical reactions were evaluated using EDX.

### 2.3. Electrochemical Measurements

All electrodes were prepared by casting a slurry containing 70% active material, 15% carbon (Super-P, 99.9%, Alfa Aesar), and 15% PAA (Mw 450000, Sigma Aldrich, St. Louis, MO, USA) or a poly(vinylidene fluoride) (PVDF, MW 534000, Sigma Aldrich, St. Louis, MO, USA) binder dissolved in N-Methyl-2-pyrrolidone. The cast electrodes were dried overnight in a vacuum oven at 70 °C and then transferred to an Ar glove box for cell assembly. A coin-type cell (CR2032) was used for half-cell testing. Li metal foil and polyethylene were used as the counter electrode and separating membrane, respectively. The electrolyte was 1 M LiPF<sub>6</sub> in ethylene carbonate/diethyl carbonate (EC/DEC, 1:1 v/v). The electrochemical performance of InSb and InSb–C was evaluated using a battery testing system (WBCS3000, WonATech, Seoul, South Korea). The galvanostatic charge–discharge (GCD) profile was measured from 0.01 to 2.5 V (vs. Li/Li<sup>+</sup>). Cyclic voltammetry (CV) at a scanning rate of 0.1 mV·s<sup>−1</sup> was used to characterize the electrochemical reactions of InSb with Li<sup>+</sup>. The rate capability was measured using a battery cyler (WBCS3000, WonATech, Seoul, South Korea) at current densities of 0.1, 0.5, 1, 3, 5, and 10 A·g<sup>−1</sup>. EIS (ZIVE MP1, WonATech) was measured in the frequency range from 100 kHz to 100 mHz with an AC amplitude of 10 mV.

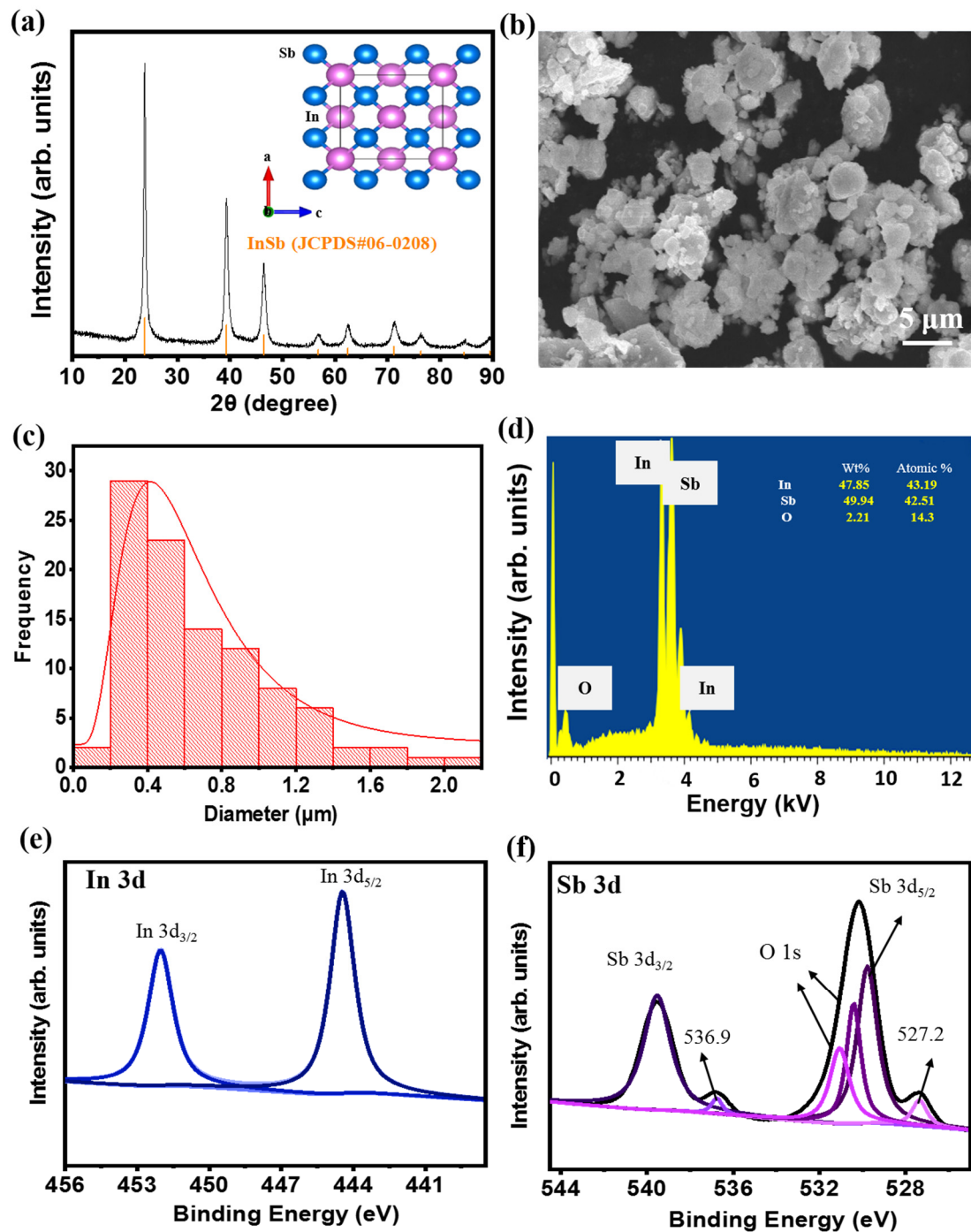
## 3. Results and Discussion

Figure 1a shows the XRD pattern of the as-prepared InSb powder obtained using the HEMM process. The XRD pattern coincided with the standard data of zinc blende InSb (JCPDS #06-0208) with no detected impurity phases. This indicated that a single phase of the zinc blende structure was successfully obtained, with a lattice constant of 0.646 Å and a space group of T<sub>d</sub><sup>2</sup>-F43 m, as shown in the inset of Figure 1a. The average crystalline domain size of the as-prepared InSb was calculated to be 0.225 nm using the Scherrer formula (Table S1). The particle size of InSb ranged from hundreds of nanometers to a few

micrometers (Figure 1b,c). One of the most important factors affecting the cell performance and safety of LIBs as well as reducing cell aging is the particle size of the active material. The particle size of the material affects the electrochemical performance of the battery [47–49]. In general, the small particles have short diffusion pathways (fast Li-ion diffusion), large surface area, and lower overpotential, thus allowing faster C-rate operation and high capacity. However, the beneficial effect of particle size reduction on cell performance is limited to certain particle sizes. The excessively large surface area can lead to large proportion of passivation layers, such as SEI, leading to an irreversible capacity loss [50–52]. Considering this, commercial batteries usually contain micrometer-sized particles for the electrode materials. However, the appropriate size of electrode material highly depends on the intrinsic properties of the electrode materials because they have different atomic structures that influence the electrochemical kinetics, Li-ion intercalation capacities, and structural stability. The size of InSb particles (mostly 200–400 nm in Figure 1c) is thought to be effective in terms of Li-ion diffusion kinetics and capacity while restraining the excessive surface passivation (e.g., SEI). EDX analysis of the InSb powder revealed that the elemental ratio of In and Sb was approximately 1:1 (Figure 1d). The presence of O in the InSb powder is due to the partially oxidized surface of the InSb particles. The composition and chemical state of InSb were examined using XPS (Figure 1e,f). The XPS signals observed at 452.1 and 444.5 eV (Figure 1e) can be ascribed to In 3d<sub>3/2</sub> and In 3d<sub>5/2</sub>, respectively, while the peaks at 539.5 and 530.1 eV (Figure 1f) were indexed to Sb 3d<sub>3/2</sub> and Sb 3d<sub>5/2</sub>, respectively, verifying the InSb alloy structure after the HEMM process. Meanwhile, the two small peaks at 536.9 and 527.2 eV (Figure 1f) are related to the surface oxidation of the InSb materials, consistent with the EDX analysis results (Figure 1d). The FTIR analysis of the InSb also confirmed the presence of hydroxide functional groups, as shown in Figure S1. The presence of hydroxyl groups on InSb should result in a high affinity for binders with polar functional groups (such as PAA), which can form strong hydrogen bonds. The binder can then serve as an elastic barrier that prevents InSb particles from aggregating while maintaining stable contact between the electrode and current collector during electrochemical reactions.

The half-cell performance of InSb was measured using two different binders (PAA and PVDF) to investigate its electrochemical behavior (Figure 2). The GCD voltage profiles of InSb\_PAA and InSb\_PVDF are shown in Figure 2a and Figure S2, respectively. The initial charge/discharge capacities of InSb\_PAA and InSb\_PVDF were 790/635 and 770/643 mAh·g<sup>-1</sup>, respectively, corresponding to initial coulombic efficiencies (ICEs) of 80.9% and 83.5%. The irreversible capacity losses in the first cycle are associated with the formation of an SEI layer for both electrodes. Although the specific capacities of InSb were not significantly different for PAA and PVDF in the first cycle, a significant capacity reduction was observed for InSb\_PVDF during the initial 10 cycles at both low (Figure 2b) and high current densities (Figure 2c). The specific capacities of InSb\_PVDF were 203.3 mAh·g<sup>-1</sup> after 140 cycles and 146.8 mAh·g<sup>-1</sup> after 100 cycles at 100 and 500 mA·g<sup>-1</sup>, respectively, corresponding to capacity retention values of 30.4% and 27.5%. Moreover, InSb\_PAA displayed much better performance in terms of stability and capacity; it exhibited specific capacities of 639.5 mAh·g<sup>-1</sup> after 140 cycles (93.2% capacity retention) and 558.3 mAh·g<sup>-1</sup> after 100 cycles (92.3% capacity retention) at 100 and 500 mA·g<sup>-1</sup>, respectively. Figure S3 displays the surface morphologies of pristine InSb\_PAA and InSb\_PVDF. InSb\_PAA showed a more uniform surface with a lower roughness than InSb\_PVDF owing to the strong hydrogen-bonding interaction between the hydroxyl groups on the InSb particles and the carboxylate groups in PAA, which is not present in InSb\_PVDF. Figure 2d shows the first five CV cycles for InSb\_PAA in the voltage range from 0.005 to 3.0 V vs. Li/Li<sup>+</sup>. The initial CV curve was markedly different from those of the subsequent cycles due to the formation of an SEI layer on the electrode surface. In the first discharge step, a significant reduction peak emerged at 0.38 V, indicating the Li intercalation into InSb to form Li<sub>2</sub>Sb and In. The peak emerging at 0.24 V can be due to the reaction between In and Li to form Li<sub>y</sub>In. Thus, after completing the discharge step, Li<sub>2</sub>Sb and Li<sub>2</sub>In appear as final products. In the charge process, three oxidation peaks were observed at voltages of 0.70, 0.98, and 1.12 V.

Among them, the first peak at 0.70 V corresponds to the complete exclusion of Li, reverting  $\text{Li}_2\text{In}$  into In. When the anode was charged to 0.98 and 1.12 V, In began to intrude into  $\text{Li}_2\text{Sb}$  to form InSb. The detailed analysis of this phase transformation will be discussed in the ex-situ analyses. However, the curves nearly overlapped after the second cycle, demonstrating the high reversibility and stability of InSb\_PAA. Compared to InSb\_PAA, InSb\_PVDF showed relatively unstable CV curves with polarized oxidation and reduction peaks even after the second cycle (Figure S4).



**Figure 1.** (a) XRD pattern (inset: crystalline structure), (b) SEM image, (c) particle size distribution, and (d) EDX spectrum of the as-synthesized InSb powder. XPS profiles of (e) In 3d, and (f) Sb 3d for the InSb powder.

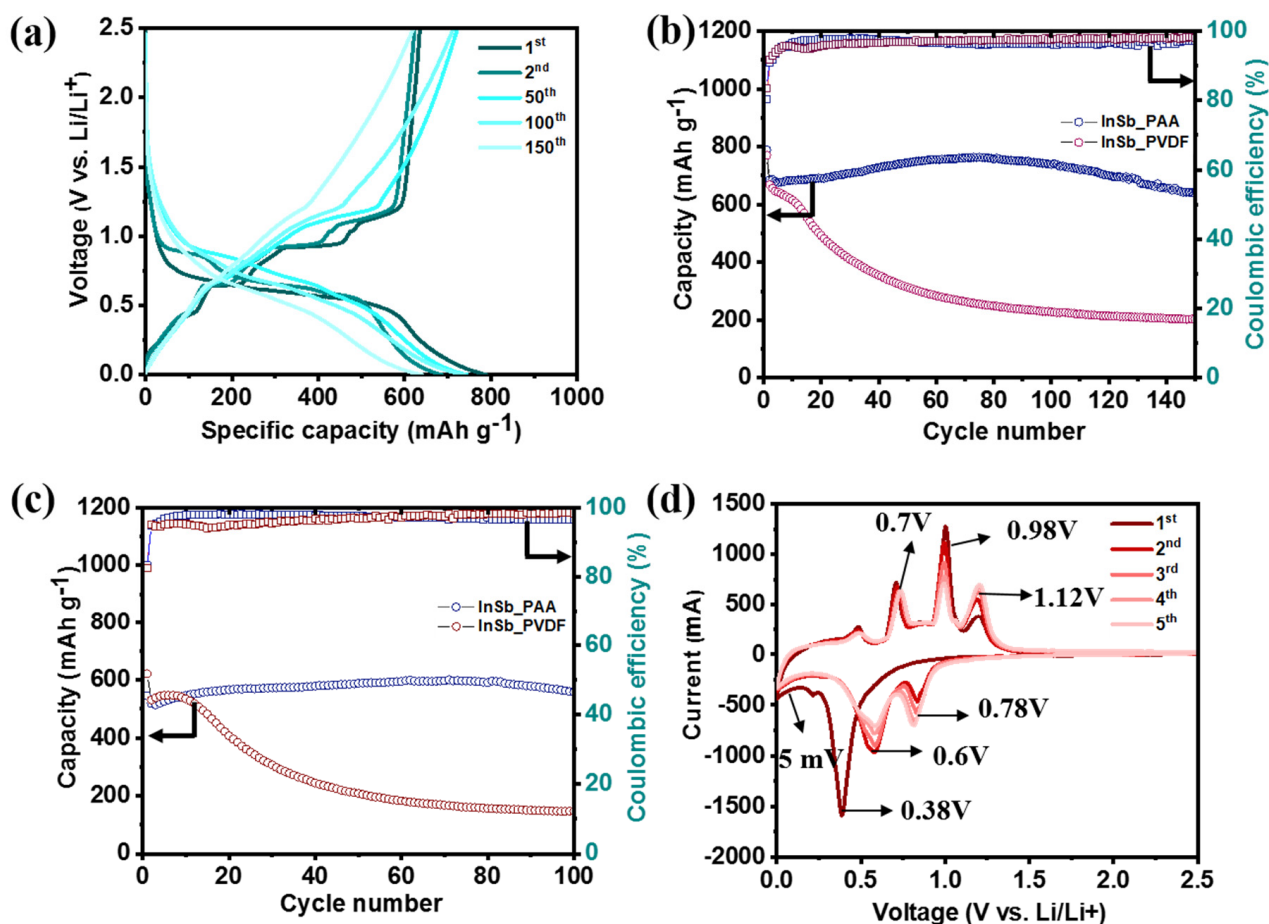


**Figure 2.** Electrochemical performance of the InSb electrode. (a) GCD voltage profiles of InSb\_PAA at a current density of  $100 \text{ mA} \cdot \text{g}^{-1}$ . Cyclic performance of the InSb\_PAA and InSb\_PVDF at a current density of (b) 100 and (c)  $500 \text{ mA} \cdot \text{g}^{-1}$ . (d) CV curves of InSb\_PAA.

Figure 3 compares the cross-sectional SEM images of InSb\_PAA and InSb\_PVDF in the pristine state and after 20 cycles. Although the thicknesses of InSb\_PAA and InSb\_PVDF were similar in the pristine states ( $10.2 \mu\text{m}$  in Figure 3a,d), InSb\_PAA was thinner ( $10.8 \mu\text{m}$  in Figure 3b) than InSb\_PVDF ( $12.4 \mu\text{m}$  in Figure 3e) after 20 cycles, indicating a smaller volume expansion of the InSb\_PAA. In addition, the InSb\_PAA maintained close contact between the electrode and current collector after 20 cycles (Figure 3c). However, the InSb\_PVDF electrode partially delaminated from the current collector (Figure 3e) and aggregated (Figure 3f), because it failed to accommodate the large volume change of the InSb particles during repeated electrochemical reactions. These results justify the selection of PAA as an appropriate binder material for the InSb electrode.

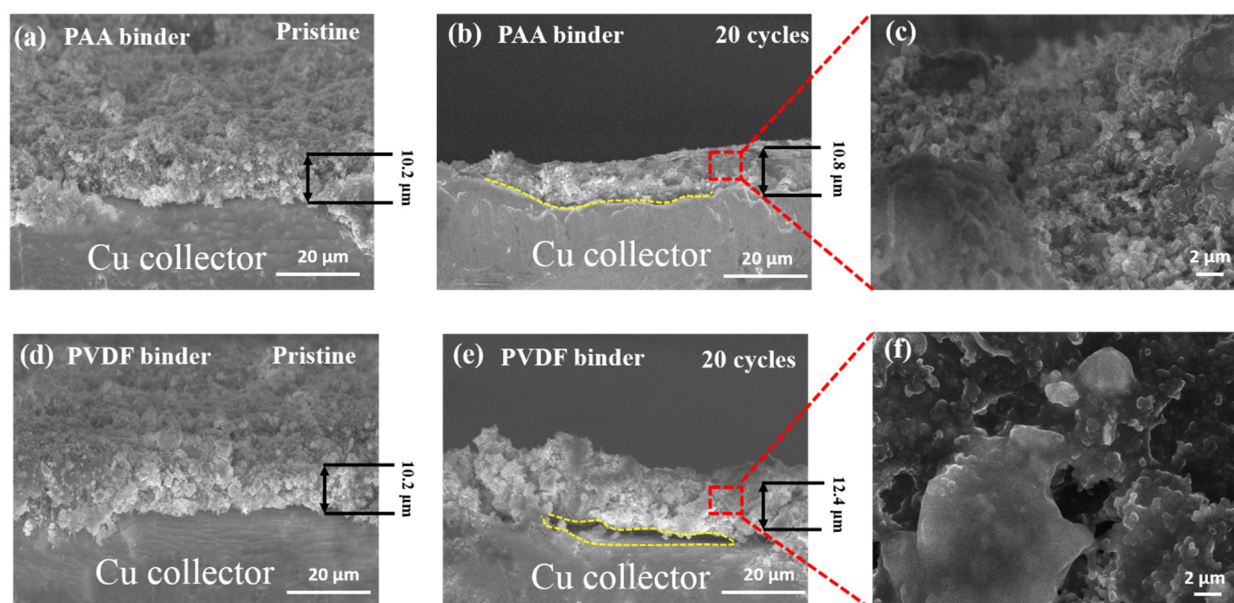
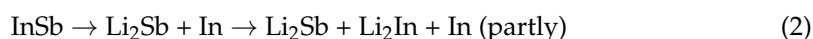


**Figure 3.** Comparison of the InSb\_PAA and InSb\_PVDF electrodes before and after 20 cycles. Cross-sectional images of (a) pristine InSb\_PAA, (b,c) InSb\_PAA after 20 cycles at different magnifications, (d) pristine InSb\_PVDF, and (e,f) InSb\_PVDF after 20 cycles at different magnifications. The dashed yellow lines in (b,e) indicate the boundary between electrode and Cu collector.

Ex-situ XRD was used to investigate the electrochemical reaction mechanism during the initial lithiation/delithiation process of the InSb electrode (Figure 4a). At a discharge voltage of 0.38 V (D-0.38 V), peaks corresponding to  $\text{Li}_2\text{Sb}$  and In emerged. When fully discharged (D-5 mV),  $\text{Li}_2\text{In}$  peaks appeared, while  $\text{Li}_2\text{Sb}$  and In peaks remained. Upon charging to 0.7 V (C-0.7 V), the  $\text{Li}_2\text{In}$  phase disappeared. At the charging states of 0.98 and 1.12 V the  $\text{Li}_2\text{Sb}$  phase vanished. When fully charged to 2.5 V (C-2.5 V), only the peaks matching with InSb re-emerged. The structural transformation of InSb during lithiation/delithiation is summarized as follows:

Discharging:



Charging:



Notably, the InSb phase (major peaks at  $39.9^\circ$  and  $46.5^\circ$ ) fully recovered without any impurity peaks after the first cycle, indicating a highly reversible reaction of InSb with Li ions. This likely correlates with the robust binding between InSb and PAA, which effectively protects the active material from pulverization and delamination caused by volume changes. The ex-situ XRD results demonstrate the conversion and alloying/dealloying mechanism of the InSb electrode during discharge/charge, as schematically illustrated in Figure 4b.

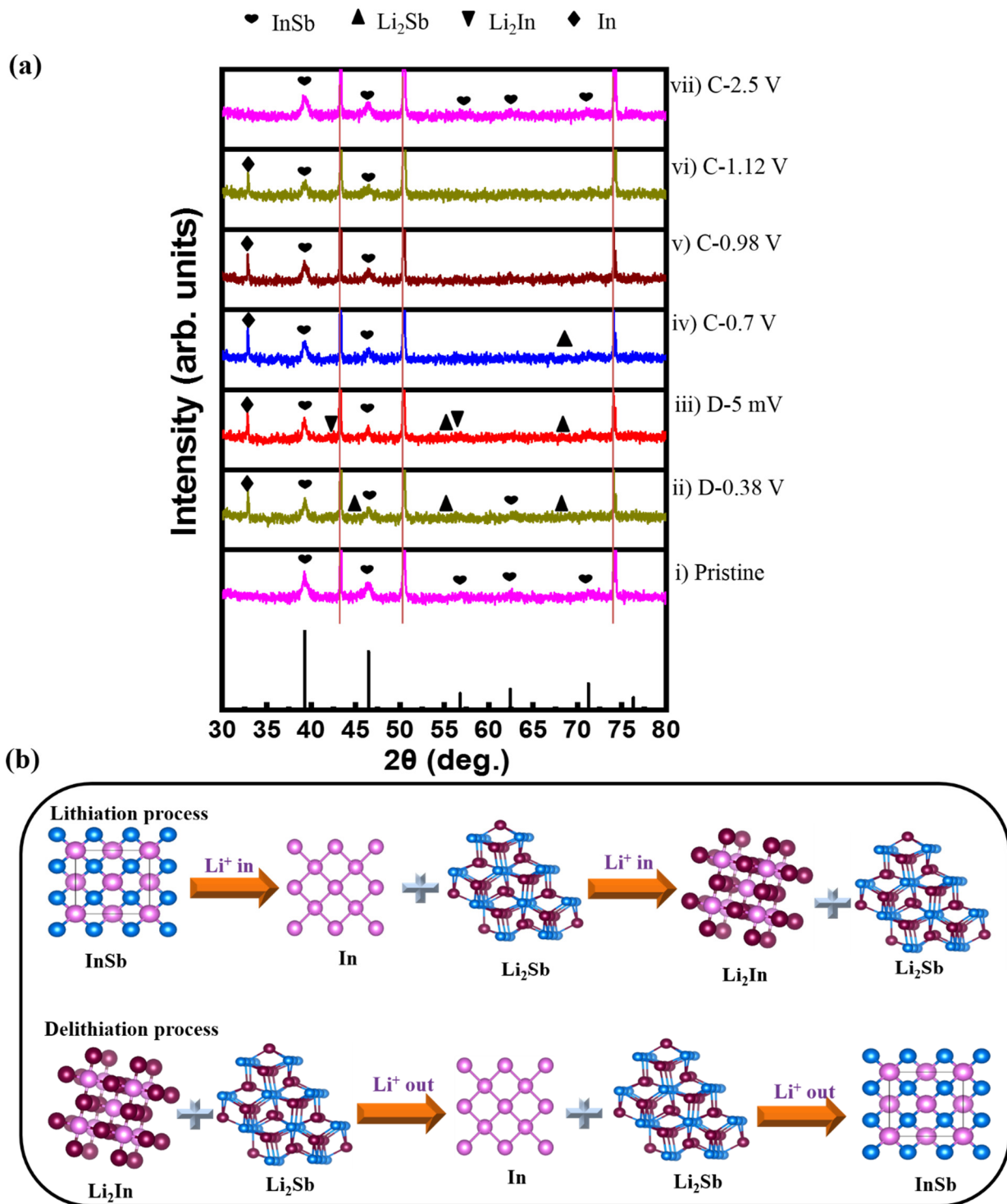


**Figure 4.** (a) XRD patterns collected at selected potential states in the initial lithiation/delithiation process. (b) Schematic of the electrochemical reaction mechanism of the InSb\_PAA electrode during cycling.

Despite the better performance of InSb\_PAA compared to that of InSb\_PVDF, the InSb\_PAA electrode still had a gradual decrease in capacity after ~80 cycles when measured at  $100 \text{ mA} \cdot \text{g}^{-1}$  (Figure 2b). This behavior is also reflected in the coulombic efficiency (CE) variation (Table S2), where the CE steadily increased until ~60 cycles, then decreased afterwards. This might be associated with increasing side reactions between InSb\_PAA and the electrolyte as the electrode was cycled. These side reactions can be further explained by a differential capacity plot (DCP) analysis of the initial 140 cycles (Figure S5). From this

analysis, the main reduction (at  $\sim 0.86$  and  $\sim 0.92$  V) and oxidation (at  $\sim 0.59$  and  $0.81$  V) peaks remained unchanged for 80 cycles, but then became broader and shifted after 80 cycles. This polarization leads to inefficient lithiation/delithiation and a progressive capacity drop after 80 cycles. A similar trend was observed at a high current density (Figure 2c). In this case, the capacity gradually increased until 80 cycles, followed by a slight decrease in subsequent cycles. This trend was also observed in the CE variation (Table S3) and DCP analysis (Figures S6 and S7), where the intensities of the oxidation (at  $\sim 0.59$  and  $0.81$  V) and reduction (at  $\sim 0.86$  and  $\sim 0.92$  V) peaks generally increased for 60 cycles with a negligible polarization (Figure S6), then decreased in intensity after 60 cycles with a slight polarization (Figure S7). Therefore, the electrochemical performance of InSb\_PAA at current densities of 100 and  $500 \text{ mA}\cdot\text{g}^{-1}$  was not fully satisfactory, based on these results.

High-performance LIB anode materials frequently use C decoration to overcome the disadvantages of the active materials. Amorphous C provides improved electrical conductivity and acts as a buffer for withstanding the volume change of Li-active materials [53–56]. Therefore, InSb–C (or InSb–C\_PAA) was prepared by two sequential steps of HEMM (adding acetylene black to the InSb electrode in the secondary HEMM). The XRD peaks of the as-prepared InSb–C matched well with those of InSb (Figure 5a). The size and shape of the InSb–C were almost unchanged compared to those of InSb (Figure 5b). The presence of InSb nanocrystallites was confirmed with HRTEM, with interplanar distances of  $0.374 \text{ nm}$  and  $0.229 \text{ nm}$  ((111) and (220) phases of InSb, respectively (Figure 5c)), which was consistent with the XRD analysis. The elemental mapping images (Sb, In, and C) revealed evenly distributed constituent elements (Figure 5d). In addition, the uniform distribution of O confirmed the oxidation of the functional groups on the InSb–C, as in the case of InSb.

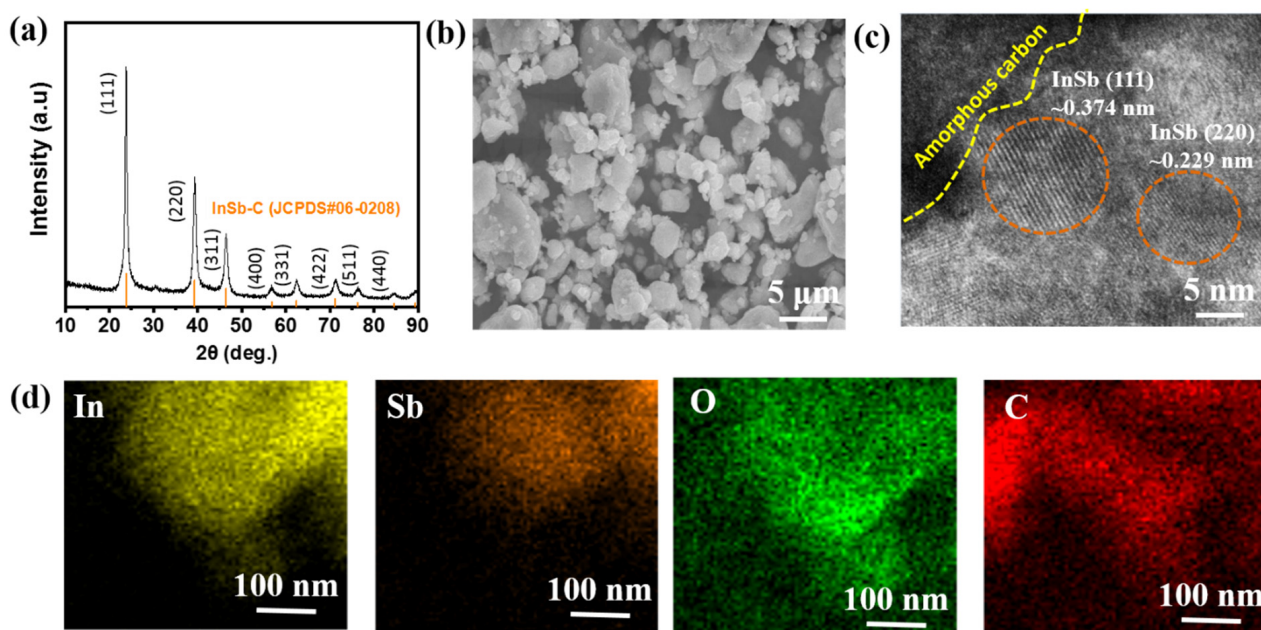


**Figure 5.** (a) XRD pattern, (b) SEM image, (c) HRTEM image, and (d) EDX elemental maps of In, Sb, O, and C of InSb–C.

The electrochemical performance of the InSb–C\_PAA electrode is shown in Figure 6. The initial charge/discharge capacity of InSb–C\_PAA was  $669/540 \text{ mAh}\cdot\text{g}^{-1}$  with an ICE of 80.7% (Figure 6a). From the EDX analysis (Figure S8) and the calculated theoretical capacity of the individual components (Table S4), the capacity contribution from C in the InSb electrode was estimated to be  $\sim 10\%$ . Therefore, the capacity of the electrode was mainly from the active InSb (90% of the total capacity) while C mainly functioned as a buffer matrix (10% capacity contribution) that mitigated the volume expansion of the electrode. Remarkably, the measured capacities of InSb\_PAA and InSb–C\_PAA were

higher than their theoretical capacities (454 and 435.6 mAh·g<sup>-1</sup>, respectively, as calculated in Table S5). This additional capacity is most likely due to electrolyte decomposition and interfacial Li-ion storage. Although the specific capacity of InSb-C\_PAA was lower than that of InSb\_PAA in the initial cycle, the long-term performance of InSb-C\_PAA was superior to that of InSb\_PAA. In particular, InSb-C\_PAA delivered 878 and 634 mAh·g<sup>-1</sup> at 100 mA·g<sup>-1</sup> (Figure 6b) and 500 mA·g<sup>-1</sup> (Figure 6c) after 150 and 300 cycles, respectively. Notably, a steady capacity increase was observed for InSb-C\_PAA during the repeated discharge/charge processes, which was attributed to the creation of a polymer-gelled film from electrolyte decomposition and interfacial Li-ion storage [57–59]. Furthermore, the variations in the DCP profiles as a function of cycle number were studied at current densities of 100 and 500 mA·g<sup>-1</sup> to better understand the steady rise in capacity (Figure S9). In the DCP curves of the InSb-C\_PAA electrodes, the overall intensity of the redox potentials increased with increasing cycle number. There was also a minor positive shift in the reduction peaks (at 0.86 and 0.92 V) and a slight negative shift in the oxidation peaks (at 0.59 and 0.81 V) in the capacity-increasing region. The degree of polarization in InSb-C\_PAA was much lower than that of InSb\_PAA (Figure S9). Figure S10 compares the CE variation in InSb-C\_PAA and InSb\_PAA at current densities of 100 and 500 mA·g<sup>-1</sup>. The detailed CE values are summarized in Table S6 (at 100 mA·g<sup>-1</sup>) and Table S7 (at 500 mA·g<sup>-1</sup>) for the InSb\_PAA, InSb\_PVDF, and InSb-C\_PAA electrodes during the first 10 cycles. As seen in Table S6, InSb-C\_PAA had a slightly lower ICE (80.58%) than the InSb\_PAA (ICE = 81.42%) and InSb\_PVDF electrodes (ICE = 83.53%). However, the CE of the InSb-C\_PAA electrode significantly increased after the first cycle, exhibiting the highest CE among the three different electrodes. This trend was also observed at high current densities (Table S7). The high CE of the InSb-C\_PAA electrode after the first cycle indicated a high reversibility of lithiation/delithiation. Figure 6d shows the first five CV curves of InSb-C\_PAA. In contrast to InSb\_PAA and InSb\_PVDF, the CV curves of InSb-C\_PAA nearly overlapped after the second cycle, exhibiting exceptional cycling stability. The redox peak positions were exactly identical to those observed for InSb\_PAA (Figure 2d), indicating that InSb is the main active material. The rate performance (Figure 6e) and normalized capacity retention (Figure 6f) of InSb-C\_PAA were measured at various current densities. The average discharge capacities of InSb-C\_PAA were 669, 660, 659, 645, 644, and 635 mAh·g<sup>-1</sup> at current densities of 0.1, 0.5, 1.0, 3.0, 5.0, and 10.0 A·g<sup>-1</sup>, respectively (Figure 6e), which were significantly greater than those of InSb\_PAA and InSb\_PVDF. Remarkably, even at a high current density of 10 A·g<sup>-1</sup>, the capacity retention of InSb-C\_PAA was as high as 98% of its initial capacity (Figure 6f). Even at the current densities higher than 10 A·g<sup>-1</sup>, InSb-C\_PAA still presented outstanding electrochemical performance with average specific capacities were 627 and 541 mAh·g<sup>-1</sup> at 15 and 20 A·g<sup>-1</sup>, respectively (Figure S11). In addition, a high-capacity retention (94.4%) was achieved when the discharge rate was returned to 0.1 A·g<sup>-1</sup> from 10 A·g<sup>-1</sup>, demonstrating the good rate performance of InSb-C\_PAA.

EIS profiles of the InSb\_PAA, InSb\_PVDF, and InSb-C\_PAA electrodes were obtained at the 1st, 5th, and 20th cycles (Figure 7). The electrolyte resistance ( $R_b$ ), SEI layer resistance ( $R_{SEI}$ ), charge-transfer resistance ( $R_{ct}$ ), interfacial double layer capacitance ( $C_{dl}$ ), constant phase element ( $C_{PE}$ ), and Warburg impedance ( $Z_w$ ) are all included in the simplified equivalent circuit depicted in Figure 7a. The compressed semi-circles in the mid-frequency region of the Nyquist plots correspond to  $R_{ct}$  at the electrode–electrolyte interface. The cells containing the electrode with the PAA binder (InSb\_PAA and InSb-C\_PAA) showed decreasing semicircles in the low-frequency region with an increase in the cycle number (from 1 to 20 cycles), indicating a gradual decrease in  $R_{ct}$  and steady stabilization of the electrode (Figure 7b,d). The  $R_{ct}$  values of InSb\_PAA and InSb-C\_PAA (Figure 7b,d) were significantly lower than that of InSb\_PVDF (Figure 7c). After 20 cycles, InSb-C\_PAA exhibited the lowest  $R_{ct}$  value among the electrodes (Table S8). These results help to explain the gradual increase in capacity and performance of the InSb-C\_PAA electrode during long-term cycling.

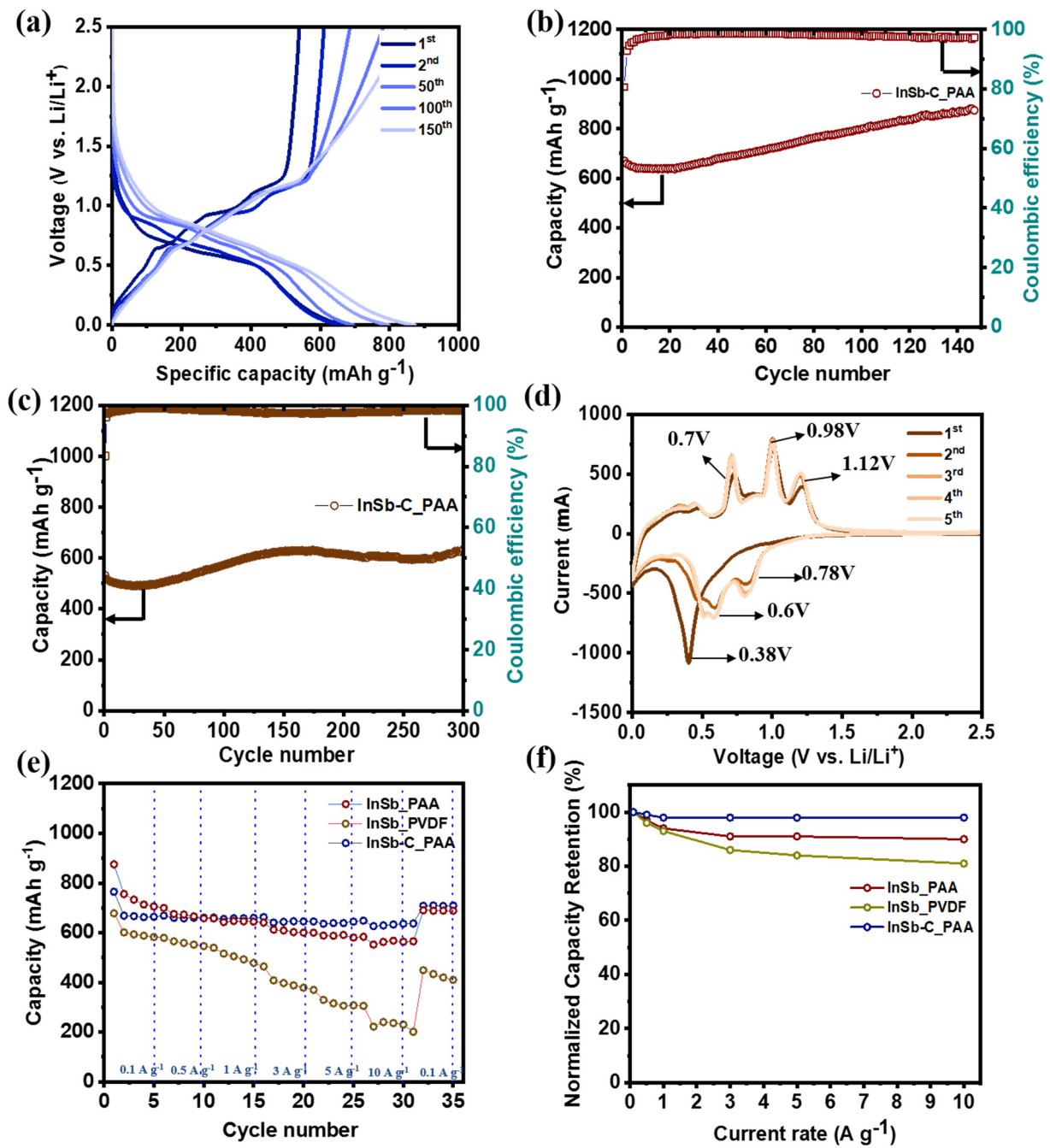


**Figure 6.** Electrochemical performance of the half-cells. (a) GCD profiles of InSb-C\_PAA at a current density of 100 mA·g<sup>-1</sup>, cyclic performance of InSb-C\_PAA at (b) 100 mA·g<sup>-1</sup> and (c) 500 mA·g<sup>-1</sup>, (d) CV curves of InSb-C\_PAA, (e) rate capabilities of the composites, and (f) capacity retention of the composites at different current densities.

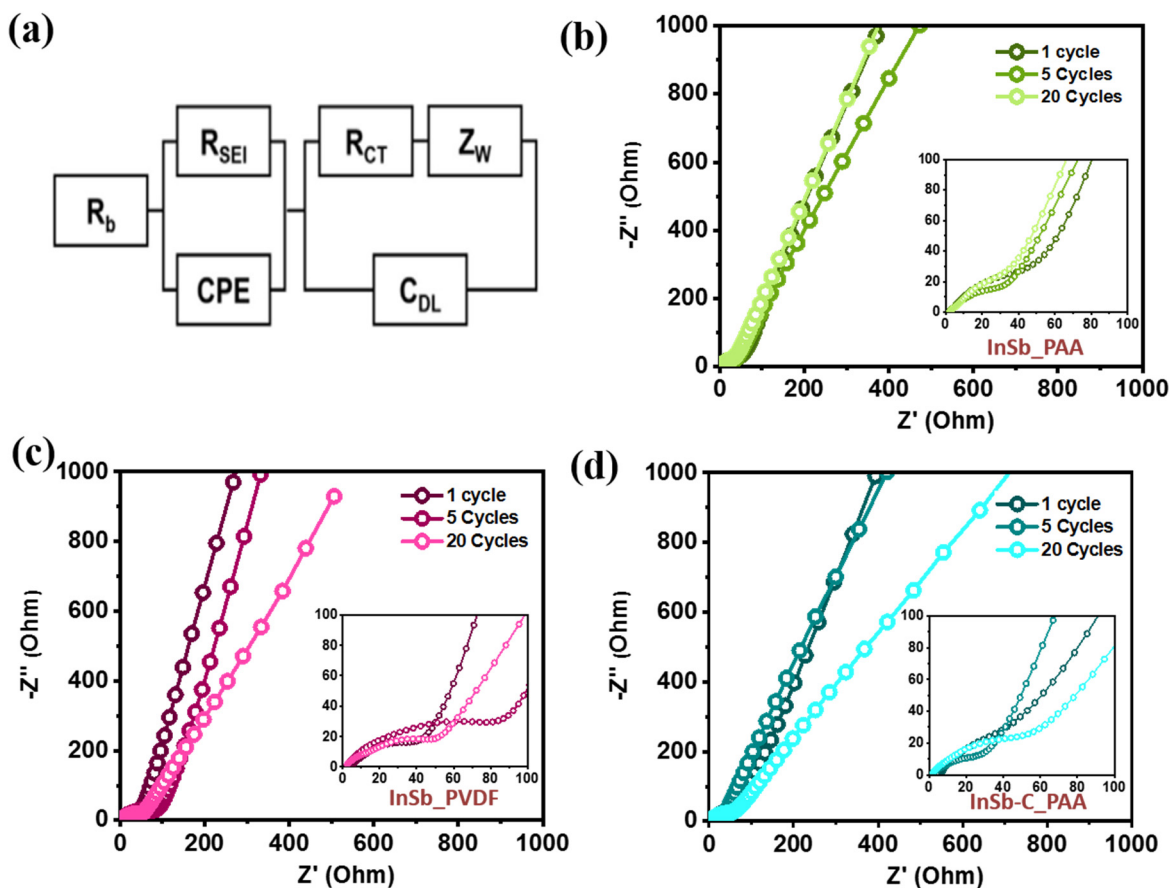


**Figure 7.** (a) The equivalent circuit. Nyquist plots after 1, 5, and 20 cycles for (b) InSb\_PAA, (c) InSb\_PVDF, and (d) InSb-C\_PAA.

Considering all the results, the Li-ion storage mechanism of the InSb-C\_PAA electrode is schematically presented in Figure 8. The overall electrochemical reaction is written as  $\text{InSb} + 4\text{Li}^+ + 4\text{e}^- \rightleftharpoons \text{Li}_2\text{Sb} + \text{Li}_2\text{In}$ , neglecting the small capacity contribution from the C matrix. As the discharge proceeds,  $\text{Li}_2\text{Sb}$  and  $\text{Li}_2\text{In}$  are formed as products after the reaction with Li ions. During this reaction, a large volume expansion ( $\text{Li}_2\text{Sb}$  (~135%) and  $\text{Li}_2\text{In}$  (~297%)) causes mechanical stress on the active InSb. Under prolonged cycles, accumulated stress can result in particle agglomeration, pulverization, and delamination. These issues were effectively resolved by employing a PAA binder and a C buffering matrix. PAA is a binder with numerous COOH functional groups that can form hydrogen bonds with OH groups on the surfaces of active materials (as determined using FTIR (Figure S1) and XPS analyses (Figure 1e)), thereby stabilizing the electrode structure. The presence of amorphous C around InSb facilitates charge transport and provides a mechanical buffer for the active InSb. Therefore, the synergistic effect between the PAA binder and amorphous C contributes to a significant improvement in the electrochemical performance of InSb. Consequently, the performance of the InSb-C\_PAA electrode is better than that of most previously reported Sb-based electrodes (Table 1).

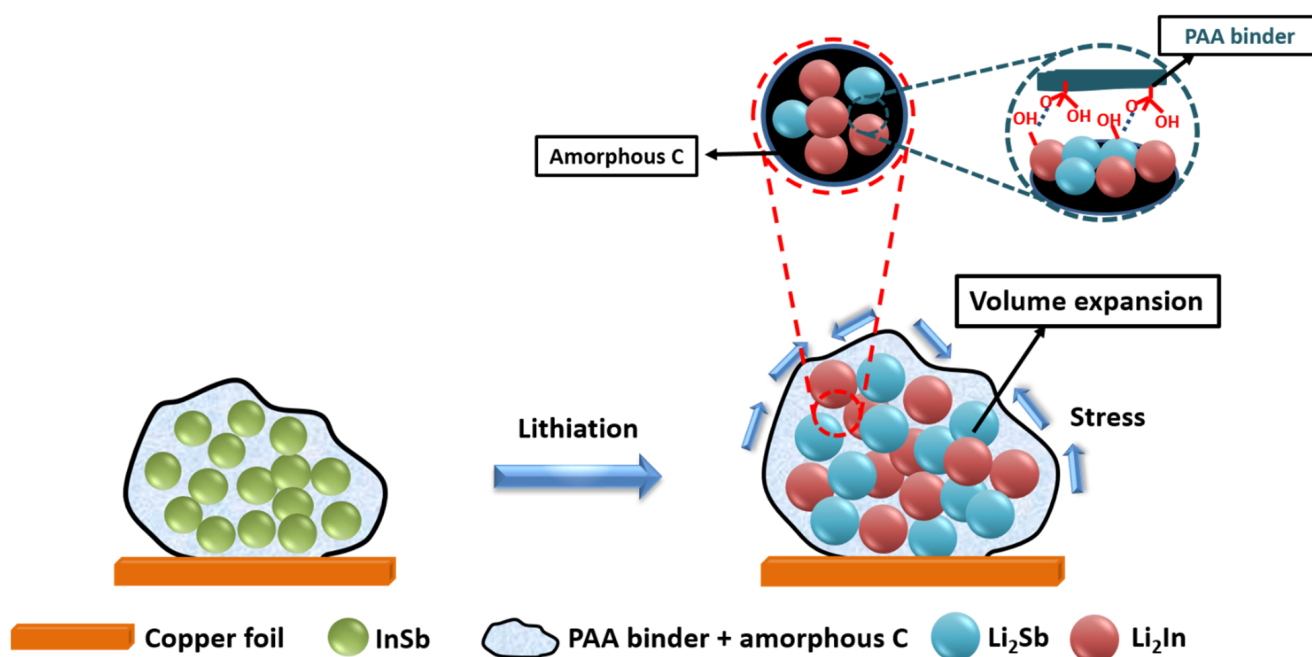


Figure 8. Illustration of the InSb–C\_PAA reaction mechanism.

Table 1. Performance comparison of intermetallic Sb-based anodes for LIBs.

Anode	Cycling Performance	Rate Capability	Synthesis Method	Ref.
Cu <sub>2</sub> Sb	290 mAh·g <sup>-1</sup> after 25 cycles	-	Ball milling	[60]
Mo <sub>3</sub> Sb <sub>7</sub>	350 mAh·g <sup>-1</sup> after 100 cycles at 0.12 C	300 mAh·g <sup>-1</sup> at 100 C	Furnace	[61]
CoSb	448 mAh·g <sup>-1</sup> after 1000 cycles at 0.66 A·g <sup>-1</sup>	-	Facile colloidal synthesis	[62]
NiSb@C	405 mAh·g <sup>-1</sup> after 1000 cycles at 0.1 A·g <sup>-1</sup>	393 mAh·g <sup>-1</sup> at 2.0 A·g <sup>-1</sup>	Freezing drying	[63]
NiSb hollow nanosphere	420 mAh·g <sup>-1</sup> after 50 cycles at 0.1 A·g <sup>-1</sup>	352 mAh·g <sup>-1</sup> at 0.8 A·g <sup>-1</sup>	Galvanic replacement reaction	[64]
NiSb/C nanosheet	393 mAh·g <sup>-1</sup> after 1000 cycles at 2 C	325 mAh·g <sup>-1</sup> at 10 C	Hydrothermal low-temperature carbothermic reduction	[65]
SnSb@Carbon fiber	674 mAh·g <sup>-1</sup> after 100 cycles at 0.1 A·g <sup>-1</sup>	163 mAh·g <sup>-1</sup> at 1.6 A·g <sup>-1</sup>	Electrospinning	[66]
ZnSb/C	481 mAh·g <sup>-1</sup> after 240 cycles at 0.1 A·g <sup>-1</sup>	426 mAh·g <sup>-1</sup> at 0.5 A·g <sup>-1</sup>	Annealing	[67]
TiSb <sub>2</sub>	240 mAh·g <sup>-1</sup> after 120 cycles at 1 C	300 mAh·g <sup>-1</sup> at 12 C	Furnace	[68]
InSb_PAA	640 mAh·g <sup>-1</sup> after 140 cycles	594 mAh·g <sup>-1</sup> at 10 A·g <sup>-1</sup>	Ball milling	This work
InSb–C_PAA	846 mAh·g <sup>-1</sup> after 150 cycles at 0.1 A·g <sup>-1</sup>	716 mAh·g <sup>-1</sup> at 10 A·g <sup>-1</sup>		

#### 4. Conclusions

In summary, InSb and InSb–C were successfully synthesized via HEMM and studied as potential anodes for LIBs. The crystal structure, morphology, and chemical state of these materials were characterized using XRD, SEM, HRTEM, EDX, and XPS. Electrochemical measurements revealed that the PAA binder played a significant role in improving the performance of the InSb-based electrode over conventional PVDF owing to the formation of hydrogen bonds with InSb, which contributed to the strong adhesion between the active materials and current collectors. The addition of amorphous C to InSb improved the mechanical stability and electrical conductivity. As a result, InSb–C\_PAA electrodes delivered a high reversible specific capacity (878 mAh·g<sup>-1</sup> at 100 mA·g<sup>-1</sup> after 140 cycles) and good rate capability (capacity retention of 98% at 10 A·g<sup>-1</sup> as compared to 0.1 A·g<sup>-1</sup>), which outperforms most of the Sb-based electrodes recently reported. The synergistic

effect of the PAA binder and amorphous C is responsible for the improved electrochemical performance of InSb–C\_PAA. Therefore, InSb–C\_PAA can be considered as a potential anode material for next-generation LIBs.

**Supplementary Materials:** The following are available online at <https://www.mdpi.com/article/10.3390/nano11123420/s1>, Figure S1: FT-IR results of InSb powder; Figure S2: GCD curves of InSb\_PVDF; Figure S3: SEM images of (a and b) InSb\_PAA, (c and d) InSb\_PVDF binder at different magnification; Figure S4: CV curves of InSb\_PVDF from first to fifth cycle; Figure S5: DCP of InSb\_PAA during 140 cycles measured at  $100 \text{ mA}\cdot\text{g}^{-1}$ : (a) 1–60 cycle, (b) 80–140 cycle. Enlarged view of (c) reduction peak and (d) oxidation peak; Figure S6: (a) DCP of InSb\_PAA during initial 60 cycles measured at  $500 \text{ mA}\cdot\text{g}^{-1}$ . Enlarged view of (b) oxidation peak and (c) reduction peak; Figure S7: (a) DCP of InSb\_PAA from 60 th to 100 th cycle measured at  $500 \text{ mA}\cdot\text{g}^{-1}$ . Enlarged view of (b) oxidation peak and (c) reduction peak; Figure S8: EDX spectrum of synthesized InSb–C; Figure S9: DCP profiles of InSb–C\_PAA electrodes at current density of (a)  $100 \text{ mA}\cdot\text{g}^{-1}$  during 140 cycles and (b)  $500 \text{ mA}\cdot\text{g}^{-1}$  during 300 cycles; Figure S10: Coulombic efficiency of InSb\_PAA, InSb\_PVDF, and InSb–C\_PAA at current density of (a) 100 and (b)  $500 \text{ mA}\cdot\text{g}^{-1}$ ; Figure S11: Cyclic performance of InSb–C\_PAA at  $15 \text{ A}\cdot\text{g}^{-1}$  and  $20 \text{ A}\cdot\text{g}^{-1}$ ; Table S1: Crystallite size of InSb calculated using Scherrer equation; Table S2: Coulombic efficiency variation of InSb\_PAA at various cycle numbers measured at  $100 \text{ mA}\cdot\text{g}^{-1}$ ; Table S3: Coulombic efficiency variation of InSb\_PAA at various cycle numbers measured at  $500 \text{ mA}\cdot\text{g}^{-1}$ ; Table S4: Calculation of capacity contribution of InSb and C in the InSb–C composite; Table S5: Calculation of theoretical capacity of InSb and InSb–C; Table S6: Coulombic efficiency of InSb\_PAA, InSb\_PVDF, and InSb–C\_PAA at current density of  $100 \text{ mA}\cdot\text{g}^{-1}$  for initial 10 cycles; Table S7: Coulombic efficiency of InSb\_PAA, InSb\_PVDF, and InSb–C\_PAA at current density of  $500 \text{ mA}\cdot\text{g}^{-1}$  for initial 10 cycles; Table S8: The charge-transfer resistance ( $R_{ct}$ ) of InSb\_PAA, InSb\_PVDF, InSb–C\_PAA.

**Author Contributions:** Conceptualization, J.H. and I.T.K.; validation, V.P.H.H.; investigation, V.P.H.H.; writing—original draft preparation, V.P.H.H.; writing—review and editing, J.H. and I.T.K.; supervision, J.H. and I.T.K.; funding acquisition, J.H. All authors have read and agreed to the published version of the manuscript.

**Funding:** This work was supported by the Basic Science Research Capacity Enhancement Project through Korea Basic Science Institute (National Research Facilities and Equipment Center) grant funded by the Ministry of Education (2019R1A6C1010016) and the Korea Institute of Energy Technology Evaluation and Planning (KETEP) and the Ministry of Trade, Industry & Energy (MOTIE) of the Republic of Korea (No. 20194030202290).

**Institutional Review Board Statement:** Not applicable.

**Informed Consent Statement:** Not applicable.

**Data Availability Statement:** Not applicable.

**Conflicts of Interest:** The authors declare no competing interest.

## References

1. Chen, T.; Jin, Y.; Lv, H.; Yang, A.; Liu, M.; Chen, B.; Xie, Y.; Chen, Q. Applications of lithium-ion batteries in grid-scale energy storage systems. *Trans. Tianjin Univ.* **2020**, *26*, 208–217. [[CrossRef](#)]
2. Armand, M.; Tarascon, J.-M. Building better batteries. *Nature* **2008**, *451*, 652–657. [[CrossRef](#)]
3. Xu, J.; Wang, D.; Kong, S.; Li, R.; Hong, Z.; Huang, F.Q. Pyrochlore phase  $\text{Ce}_2\text{Sn}_2\text{O}_7$  via an atom-confining strategy for reversible lithium storage. *J. Mater. Chem. A* **2020**, *8*, 5744–5749. [[CrossRef](#)]
4. Kim, T.; Song, W.; Son, D.-Y.; Ono, L.K.; Qi, Y. Lithium-ion batteries: Outlook on present, future, and hybridized technologies. *J. Mater. Chem. A* **2019**, *7*, 2942–2964. [[CrossRef](#)]
5. Meng, J.; Guo, H.; Niu, C.; Zhao, Y.; Xu, L.; Li, Q.; Mai, L. Advances in structure and property optimizations of battery electrode materials. *Joule* **2017**, *1*, 522–547. [[CrossRef](#)]
6. Goriparti, S.; Miele, E.; De Angelis, F.; Di Fabrizio, E.; Zaccaria, R.P.; Capiglia, C. Review on recent progress of nanostructured anode materials for Li-ion batteries. *J. Power Sources* **2014**, *257*, 421–443. [[CrossRef](#)]
7. Jiao, X.; Liu, Y.; Li, B.; Zhang, W.; He, C.; Zhang, C.; Yu, Z.; Gao, T.; Song, J. Amorphous phosphorus-carbon nanotube hybrid anode with ultralong cycle life and high-rate capability for lithium-ion batteries. *Carbon* **2019**, *148*, 518–524. [[CrossRef](#)]

8. Mun, Y.S.; Pham, T.N.; Bui, V.K.H.; Tanaji, S.T.; Lee, H.U.; Lee, G.-W.; Choi, J.S.; Kim, I.T.; Lee, Y.-C. Tin oxide evolution by heat-treatment with tin-aminoclay (SnAC) under argon condition for lithium-ion battery (LIB) anode applications. *J. Power Sources* **2019**, *437*, 226946. [[CrossRef](#)]
9. Nguyen, T.L.; Park, D.; Kim, I.T.  $\text{Fe}_x\text{Sn}_y\text{O}_z$  composites as anode materials for lithium-ion storage. *J. Nanosci. Nanotechnol.* **2019**, *19*, 6636–6640. [[CrossRef](#)] [[PubMed](#)]
10. Nguyen, T.L.; Kim, J.H.; Kim, I.T. Electrochemical performance of Sn/SnO/Ni<sub>3</sub>Sn composite anodes for lithium-ion batteries. *J. Nanosci. Nanotechnol.* **2019**, *19*, 1001–1005. [[CrossRef](#)]
11. Pham, T.N.; Tanaji, S.T.; Choi, J.S.; Lee, H.U.; Kim, I.T.; Lee, Y.C. Preparation of Sn-aminoclay (SnAC)-templated Fe<sub>3</sub>O<sub>4</sub> nanoparticles as an anode material for lithium-ion batteries. *RSC Adv.* **2019**, *9*, 10536–10545. [[CrossRef](#)]
12. Nguyen, T.; Kim, I. Ag nanoparticle-decorated MoS<sub>2</sub> nanosheets for enhancing electrochemical performance in lithium storage. *Nanomaterials* **2021**, *11*, 626. [[CrossRef](#)] [[PubMed](#)]
13. Nguyen, T.P.; Kim, I.T. Self-assembled few-layered MoS<sub>2</sub> on SnO<sub>2</sub> anode for enhancing lithium-ion storage. *Nanomaterials* **2020**, *10*, 2558. [[CrossRef](#)]
14. Preman, A.N.; Lee, H.; Yoo, J.; Kim, I.T.; Saito, T.; Ahn, S.-K. Progress of 3D network binders in silicon anodes for lithium ion batteries. *J. Mater. Chem. A* **2020**, *8*, 25548–25570. [[CrossRef](#)]
15. Nguyen, T.P.; Kim, I.T. W<sub>2</sub>C/WS<sub>2</sub> alloy nanoflowers as anode materials for lithium-ion storage. *Nanomaterials* **2020**, *10*, 1336. [[CrossRef](#)] [[PubMed](#)]
16. Kim, W.S.; Vo, T.N.; Kim, I.T. GeTe-TiC-C composite anodes for li-ion storage. *Materials* **2020**, *13*, 4222. [[CrossRef](#)]
17. Vo, T.N.; Kim, D.S.; Mun, Y.S.; Lee, H.J.; Ahn, S.-K.; Kim, I.T. Fast charging sodium-ion batteries based on Te-P-C composites and insights to low-frequency limits of four common equivalent impedance circuits. *Chem. Eng. J.* **2020**, *398*, 125703. [[CrossRef](#)]
18. Park, C.-M.; Kim, J.-H.; Kim, H.; Sohn, H.-J. Li-alloy based anode materials for Li secondary batteries. *Chem. Soc. Rev.* **2010**, *39*, 3115–3141. [[CrossRef](#)]
19. Obrovac, M.N.; Chevrier, V.L. Alloy negative electrodes for li-ion batteries. *Chem. Rev.* **2014**, *114*, 11444–11502. [[CrossRef](#)]
20. Lai, S.Y.; Knudsen, K.D.; Sejersted, B.T.; Ulvestad, A.; Mæhlen, J.P.; Kozlov, A.Y. Silicon nanoparticle ensembles for lithium-ion batteries elucidated by small-angle neutron scattering. *ACS Appl. Energy Mater.* **2019**, *2*, 3220–3227. [[CrossRef](#)]
21. Sun, Y.; Wang, L.; Li, Y.; Li, Y.; Lee, H.R.; Pei, A.; He, X.; Cui, Y. Design of red phosphorus nanostructured electrode for fast-charging lithium-ion batteries with high energy density. *Joule* **2019**, *3*, 1080–1093. [[CrossRef](#)]
22. Liu, S.; Feng, J.; Bian, X.; Qian, Y.; Liu, J.; Xu, H. Nanoporous germanium as high-capacity lithium-ion battery anode. *Nano Energy* **2015**, *13*, 651–657. [[CrossRef](#)]
23. Wang, L.; Wang, Y.; Xia, Y. A high performance lithium-ion sulfur battery based on a Li<sub>2</sub>S cathode using a dual-phase electrolyte. *Energy Environ. Sci.* **2015**, *8*, 1551–1558. [[CrossRef](#)]
24. Nam, K.-H.; Park, C.-M. Layered Sb<sub>2</sub>Te<sub>3</sub> and its nanocomposite: A new and outstanding electrode material for superior rechargeable Li-ion batteries. *J. Mater. Chem. A* **2016**, *4*, 8562–8565. [[CrossRef](#)]
25. Hou, H.; Jing, M.; Yang, Y.; Zhu, Y.; Fang, L.; Song, W.; Pan, C.; Yang, X.; Ji, X. Sodium/lithium storage behavior of antimony hollow nanospheres for rechargeable batteries. *ACS Appl. Mater. Interfaces* **2014**, *6*, 16189–16196. [[CrossRef](#)] [[PubMed](#)]
26. Luo, W.; Li, F.; Gaumet, J.-J.; Magri, P.; Diliberto, S.; Zhou, L.; Mai, L. Bottom-up confined synthesis of nanorod-in-nanotube structured Sb–N–C for durable lithium and sodium storage. *Adv. Energy Mater.* **2018**, *8*, 1703237. [[CrossRef](#)]
27. Nam, K.-H.; Park, C.-M. 2D layered Sb<sub>2</sub>Se<sub>3</sub>-based amorphous composite for high-performance Li- and Na-ion battery anodes. *J. Power Sources* **2019**, *433*, 126639. [[CrossRef](#)]
28. Darwiche, A.; Marino, C.; Sougrati, M.T.; Fraise, B.; Stievano, L.; Monconduit, L. Better cycling performances of bulk Sb in Na-Ion batteries compared to Li-Ion Systems: An unexpected electrochemical mechanism. *J. Am. Chem. Soc.* **2012**, *134*, 20805–20811. [[CrossRef](#)]
29. Yi, Z.; Han, Q.; Geng, D.; Wu, Y.; Cheng, Y.; Wang, L. One-pot chemical route for morphology-controllable fabrication of Sn-Sb micro/nano-structures: Advanced anode materials for lithium and sodium storage. *J. Power Sources* **2017**, *342*, 861–871. [[CrossRef](#)]
30. Hou, H.; Jing, M.; Yang, Y.; Zhang, Y.; Song, W.; Yang, X.; Chen, J.; Chen, Q.; Ji, X. Antimony nanoparticles anchored on interconnected carbon nanofibers networks as advanced anode material for sodium-ion batteries. *J. Power Sources* **2015**, *284*, 227–235. [[CrossRef](#)]
31. Liu, Z.; Yu, X.-Y.; Lou, X.W.; Paik, U. Sb–C coaxial nanotubes as a superior long-life and high-rate anode for sodium ion batteries. *Energy Environ. Sci.* **2016**, *9*, 2314–2318. [[CrossRef](#)]
32. Zhao, X.; Vail, S.A.; Lu, Y.; Song, J.; Pan, W.; Evans, D.R.; Lee, J.-J. Antimony/graphitic carbon composite anode for high-performance sodium-ion batteries. *ACS Appl. Mater. Interfaces* **2016**, *8*, 13871–13878. [[CrossRef](#)]
33. Yi, Z.; Han, Q.; Zan, P.; Wu, Y.; Cheng, Y.; Wang, L. Sb nanoparticles encapsulated into porous carbon matrixes for high-performance lithium-ion battery anodes. *J. Power Sources* **2016**, *331*, 16–21. [[CrossRef](#)]
34. Yang, Q.; Zhou, J.; Zhang, G.; Guo, C.; Li, M.; Zhu, Y.; Qian, Y. Sb nanoparticles uniformly dispersed in 1-D N-doped porous carbon as anodes for Li-ion and Na-ion batteries. *J. Mater. Chem. A* **2017**, *5*, 12144–12148. [[CrossRef](#)]
35. Wan, F.; Guo, J.-Z.; Zhang, X.-H.; Zhang, J.-P.; Sun, H.-Z.; Yan, Q.; Han, D.-X.; Niu, L.; Wu, X.-L. In situ binding Sb nanospheres on graphene via oxygen bonds as superior anode for ultrafast sodium-ion batteries. *ACS Appl. Mater. Interfaces* **2016**, *8*, 7790–7799. [[CrossRef](#)] [[PubMed](#)]

36. Yang, C.; Li, W.; Yang, Z.; Gu, L.; Yu, Y. Nanoconfined antimony in sulfur and nitrogen co-doped three-dimensionally (3D) interconnected macroporous carbon for high-performance sodium-ion batteries. *Nano Energy* **2015**, *18*, 12–19. [[CrossRef](#)]
37. Yim, T.; Choi, S.J.; Jo, Y.N.; Kim, T.-H.; Kim, K.J.; Jeong, G.; Kim, Y.-J. Effect of binder properties on electrochemical performance for silicon-graphite anode: Method and application of binder screening. *Electrochim. Acta* **2014**, *136*, 112–120. [[CrossRef](#)]
38. Choi, S.; Kwon, T.-W.; Coskun, A.; Choi, J.W. Highly elastic binders integrating polyrotaxanes for silicon microparticle anodes in lithium ion batteries. *Science* **2017**, *357*, 279–283. [[CrossRef](#)] [[PubMed](#)]
39. Wu, M.; Xiao, X.; Vukmirovic, N.; Xun, S.; Das, P.K.; Song, X.; Olalde-Velasco, P.; Wang, D.; Weber, A.Z.; Wang, L.-W.; et al. Toward an ideal polymer binder design for high-capacity battery anodes. *J. Am. Chem. Soc.* **2013**, *135*, 12048–12056. [[CrossRef](#)] [[PubMed](#)]
40. Koo, B.; Kim, H.; Cho, Y.; Lee, K.T.; Choi, N.-S.; Cho, J. A highly cross-linked polymeric binder for high-performance silicon negative electrodes in lithium ion batteries. *Angew. Chem. Int. Ed.* **2012**, *51*, 8762–8767. [[CrossRef](#)]
41. Mazouzi, D.; Karkar, Z.; Hernandez, C.R.; Manero, P.J.; Guyomard, D.; Roué, L.; Lestriez, B. Critical roles of binders and formulation at multiscales of silicon-based composite electrodes. *J. Power Sources* **2015**, *280*, 533–549. [[CrossRef](#)]
42. Magasinski, A.; Zdyrko, B.; Kovalenko, I.; Hertzberg, B.; Burtovyy, R.; Huebner, C.F.; Fuller, T.F.; Luzinov, I.; Yushin, G. Toward efficient binders for Li-Ion battery Si-Based anodes: Polyacrylic acid. *ACS Appl. Mater. Interfaces* **2010**, *2*, 3004–3010. [[CrossRef](#)] [[PubMed](#)]
43. Key, B.; Bhattacharyya, R.; Morcrette, M.; Seznéc, V.; Tarascon, J.-M.; Grey, C. Real-time NMR investigations of structural changes in silicon electrodes for Lithium-Ion batteries. *J. Am. Chem. Soc.* **2009**, *131*, 9239–9249. [[CrossRef](#)]
44. Madelung, O.; Rössler, U.; Schulz, M. Indium antimonide (InSb), carrier concentrations: Datasheet from Landolt-Börnstein—Group III Condensed Matter Volume 41A1β. In *Group IV Elements, IV-IV and III-V Compounds. Part b-Electronic, Transport, Optical and Other Properties*; Springer: Berlin, Germany, 2002; pp. 1–6. [[CrossRef](#)]
45. Isaacson, R.A. Electron spin resonance in n-Type InSb. *Phys. Rev.* **1968**, *169*, 312–314. [[CrossRef](#)]
46. Orlov, V.G.; Sergeev, G. Numerical simulation of the transport properties of indium antimonide. *Phys. Solid State* **2013**, *55*, 2215–2222. [[CrossRef](#)]
47. Agubra, V.; Fergus, J. Lithium ion battery anode aging mechanisms. *Materials* **2013**, *6*, 1310–1325. [[CrossRef](#)]
48. Joho, F.; Rykart, B.; Blome, A.; Novák, P.; Wilhelm, H.; Spahr, M.E. Relation between surface properties, pore structure and first-cycle charge loss of graphite as negative electrode in lithium-ion batteries. *J. Power Sources* **2001**, *97*, 78–82. [[CrossRef](#)]
49. Tran, T.D.; Feikert, J.H.; Pekala, R.W.; Kinoshita, K. Rate effect on lithium-ion graphite electrode performance. *J. Appl. Electrochem.* **1996**, *26*, 1161–1167. [[CrossRef](#)]
50. Bläubaum, L.; Röder, F.; Nowak, C.; Chan, H.S.; Kwade, A.; Krewer, U. Impact of particle size distribution on performance of Lithium-Ion batteries. *ChemElectroChem* **2020**, *7*, 4755–4766. [[CrossRef](#)]
51. Roselin, L.S.; Juang, R.-S.; Hsieh, C.-T.; Sagadevan, S.; Umar, A.; Selvin, R.; Hegazy, H.H. Recent advances and perspectives of carbon-based nanostructures as anode materials for Li-ion batteries. *Materials* **2019**, *12*, 1229. [[CrossRef](#)]
52. Röder, F.; Braatz, R.D.; Krewer, U. Multi-scale simulation of heterogeneous surface film growth mechanisms in Lithium-Ion batteries. *J. Electrochem. Soc.* **2017**, *164*, E3335–E3344. [[CrossRef](#)]
53. Dong, Y.; Yang, S.; Zhang, Z.; Lee, J.-M.; Zapien, J.A. Enhanced electrochemical performance of lithium ion batteries using Sb<sub>2</sub>S<sub>3</sub> nanorods wrapped in graphene nanosheets as anode materials. *Nanoscale* **2018**, *10*, 3159–3165. [[CrossRef](#)]
54. Wang, X.; Hwang, J.-Y.; Myung, S.-T.; Hassoun, J.; Sun, Y.-K. Graphene decorated by indium sulfide nanoparticles as high-performance anode for sodium-ion batteries. *ACS Appl. Mater. Interfaces* **2017**, *9*, 23723–23730. [[CrossRef](#)] [[PubMed](#)]
55. Ganesan, V.; Nam, K.-H.; Park, C.-M. Robust polyhedral CoTe<sub>2</sub>-C nanocomposites as high-performance Li- and Na-Ion battery anodes. *ACS Appl. Energy Mater.* **2020**, *3*, 4877–4887. [[CrossRef](#)]
56. Zhang, W.; Zhang, Q.; Shi, Q.; Xin, S.; Wu, J.; Zhang, C.-L.; Qiu, L.; Zhang, C. Facile synthesis of carbon-coated porous Sb<sub>2</sub>Te<sub>3</sub> nanoplates with high alkali metal ion storage. *ACS Appl. Mater. Interfaces* **2019**, *11*, 29934–29940. [[CrossRef](#)] [[PubMed](#)]
57. Kang, W.; Tang, Y.; Li, W.; Yang, X.; Xue, H.; Yang, Q.; Lee, C.S. High interfacial storage capability of porous NiMn<sub>2</sub>O<sub>4</sub>/C hierarchical tremella-like nanostructures as the Lithium-Ion battery anode. *Nanoscale* **2015**, *7*, 225–231. [[CrossRef](#)]
58. Zeng, Z.; Zhao, H.; Lv, P.; Zhang, Z.; Wang, J.; Xia, Q. Electrochemical properties of iron oxides/carbon nanotubes as anode material for lithium ion batteries. *J. Power Sources* **2015**, *274*, 1091–1099. [[CrossRef](#)]
59. Zhu, X.J.; Guo, Z.P.; Zhang, P.; Du, G.D.; Zeng, R.; Chen, Z.X.; Li, S.; Liu, H.K. Highly porous reticular tin-cobalt oxide composite thin film anodes for lithium ion batteries. *J. Mater. Chem.* **2009**, *19*, 8360–8365. [[CrossRef](#)]
60. Fransson, L.; Vaughey, J.; Benedek, R.; Edström, K.; Thomas, J.; Thackeray, M. Phase transitions in lithiated Cu<sub>2</sub>Sb anodes for lithium batteries: An in situ X-ray diffraction study. *Electrochem. Commun.* **2001**, *3*, 317–323. [[CrossRef](#)]
61. Baggetto, L.; Allcorn, E.; Unocic, R.R.; Manthiram, A.; Veith, G.M. Mo<sub>3</sub>Sb<sub>7</sub> as a very fast anode material for lithium-ion and sodium-ion batteries. *J. Mater. Chem. A* **2013**, *1*, 11163–11169. [[CrossRef](#)]
62. Wang, S.; He, M.; Walter, M.; Kravchuk, K.V.; Kovalenko, M.V. Monodisperse CoSb nanocrystals as high-performance anode material for Li-ion batteries. *Chem. Commun.* **2020**, *56*, 13872–13875. [[CrossRef](#)]
63. Pan, Q.; Wu, Y.; Zhong, W.; Zheng, F.; Li, Y.; Liu, Y.; Hu, J.; Yang, C. Carbon nanosheets encapsulated NiSb nanoparticles as advanced anode materials for Lithium-Ion batteries. *Energy Environ. Mater.* **2020**, *3*, 186–191. [[CrossRef](#)]
64. Hou, H.; Cao, X.; Yang, Y.; Fang, L.; Pan, C.; Yang, X.; Song, W.; Ji, X. NiSb alloy hollow nanospheres as anode materials for rechargeable lithium ion batteries. *Chem. Commun.* **2014**, *50*, 8201–8203. [[CrossRef](#)] [[PubMed](#)]

65. Song, G.; Choi, S.; Hwang, C.; Ryu, J.; Song, W.-J.; Song, H.-K.; Park, S. Rational structure design of fast-charging NiSb Bimetal nanosheet anode for Lithium-ion batteries. *Energy Fuels* **2020**, *34*, 10211–10217. [[CrossRef](#)]
66. Ning, X.; Li, Z. Centrifugally spun SnSb nanoparticle/porous carbon fiber composite as high-performance lithium-ion battery anode. *Mater. Lett.* **2021**, *287*, 129298. [[CrossRef](#)]
67. Fan, L.; Liu, Y.; Tamirat, A.G.; Wang, Y.; Xia, Y. Synthesis of ZnSb@C microflower composites and their enhanced electrochemical performance for lithium-ion and sodium-ion batteries. *New J. Chem.* **2017**, *41*, 13060–13066. [[CrossRef](#)]
68. Gómez-Cámer, J.L.; Novák, P. Polyacrylate bound TiSb<sub>2</sub> electrodes for Li-ion batteries. *J. Power Sources* **2015**, *273*, 174–179. [[CrossRef](#)]